CsₓWO₃ Nanorods Coated with Polyelectrolyte Multilayers as a Multifunctional Nanomaterial for Bimodal Imaging-Guided Photothermal/Photodynamic Cancer Treatment

Wei Guo, Chongshen Guo,* Nannan Zheng, Tiedong Sun, and Shaoqin Liu*

Activatable theranostics that combines multimodality imaging and therapy has drawn extensive attention for biomedical applications because synergy achieved through multimodality imaging could provide highly complementary and more accurate information, enabling us to better track the involved physiological and pathological process in region of interest as well as analyze the treatment efficacy.[1] For example, radioactive ^{64}Cu-intergrated Au nanomaterials provided an accurate and sensitive localization of nanomaterials through noninvasive positron emission tomography (PET) imaging were successfully used for PET image-guided photothermal therapy.[1f] Among various multimodality imaging techniques, the dual-imaging modalities of X-ray computed tomography (CT)/ photoacoustic imaging tomography (PAT) have attracted special interest in accurate disease diagnosis. The reason lies in the fact that CT imaging has advantages in 3D whole-body image and deep tissue penetration,[2] while PAT is characteristic of high spatial resolution, noninvasiveness, deep penetration, and accurate quantification along with the capability in guiding bulk tumor resection intraperatively.[3] Indeed, noninvasive, nonionzing PAT technique has been used for real-time intestinal functional imaging with low background and remarkable resolution.[3h] As a result, combination of CT/PAT not only provides a wealth of information about the structure (CT) as well as pathophysiological status (PAT), but also allows us to illustrate the gradual accumulation of theranostic drugs in the tumor upon either intratumoral local administration or intravenous systemic administration.[4] The fascinating characteristics of CT/PAT stimulate development and construction of efficient multimodal agents with enhanced CT and PAT contrast. However, the chemical requirement for CT and PAT contrast agents is quite different. The sensitivity of PAT imaging is determined by the conversion efficiency of light energy to a PAT pressure wave, so the exogenous PAT contrast agents must have high optical absorbance in the near infrared (NIR) region to improve the imaging sensitivity.[5] With respect to CT imaging, the enhanced X-ray contrast may be obtained by employing metal elements with a high atomic number Z > 50[6] or iodinated oil.[7] Therefore, efficient bimodal imaging probes with enhanced CT and PAT contrast should hybridize the characteristics of large NIR optical absorption and high atomic number.

Due to their strong localized surface plasmon resonance (LSPR) feature and high X-ray attenuating potency, tungsten-based nanomaterials, such as few-layered 2D tungsten dichalocogenides[8] and tungsten oxide nanoparticles,[9] have been explored as potential candidates for cancer photothermotherapy (PT)[10] and CT contrast agent.[11] Compared to traditional PT candidates,[12] tungsten oxide nanoparticles with strong absorbance in the whole NIR region would render PT therapy even using long wavelength 1064 nm laser irradiation, thus achieving deeper skin penetration and higher body tolerance.[13] However, few tungsten-based nanomaterials have been reported due to their obvious shortcomings including poor biocompatibility and difficulty in controlling the morphology and surface chemistry. Inspired by the remarkable physicochemical properties of tungsten bronze, such as high atomic number ($Z = 73$) and strong absorbance in the NIR region, in this study, we therefore develop a novel multifunctional theranostic system based on tungsten bronze, CsₓWO₃ nanorods (NRs). The surface of negatively charged CsₓWO₃ NRs is coated with positively charged polyelectrolyte multilayers via the layer-by-layer (LBL) assembly technique, which greatly improves the biocompatibility of these NRs and their uptake by the cells. The strong X-ray attenuation ability and strong NIR absorbance of the polyelectrolyte-multilayer-coated CsₓWO₃ NRs (CsₓWO₃ NR@PEM) are used for enhanced CT and PAT imaging, respectively. Meanwhile, the CsₓWO₃ NR@PEM has wide and strong optical absorption in the whole NIR range of 780–2500 nm, covering both biological windows I and II. Based on CT/PAT bimodal imaging guidance, highly effective in vivo photodynamic (PD) and PT therapy of tumors is achieved after intratumoral injection with low dose of CsₓWO₃ NR@PEM upon 880 nm (biological window I) or 1064 nm (biological window II) laser irradiation. Primary result demonstrates that the tumor elimination is caused by the photoactive hyperthermia and single oxygen generated by CsₓWO₃ NR@PEM, suggesting the promise of combined PD and PT effect using one agent. It is noteworthy that PD has been proven to be effective for oxygen-rich part (i.e., the outer part) of tumors, but it suffers severely from therapeutic deterioration as treatment time elapse owing to depletion of tissue oxygen.[14] PT ablation is highly efficient for the inner part of tumors due to heat accumulation, but PT has risks of inefficiency near large

W. Guo, N. N. Zheng, T. D. Sun, Prof. S. Q. Liu
State Key Laboratory of Urban Water Resource
and Environment
School of Life Science and Technology
Harbin Institute of Technology
Harbin 150080, China
E-mail: shaoqinliu@hit.edu.cn
W. Guo, Dr. C. S. Guo, N. N. Zheng, T. D. Sun,
Prof. S. Q. Liu
Micro- and Nanotechnology Research Center
Harbin Institute of Technology
Harbin 150080, China
E-mail: chongshenguo@hit.edu.cn

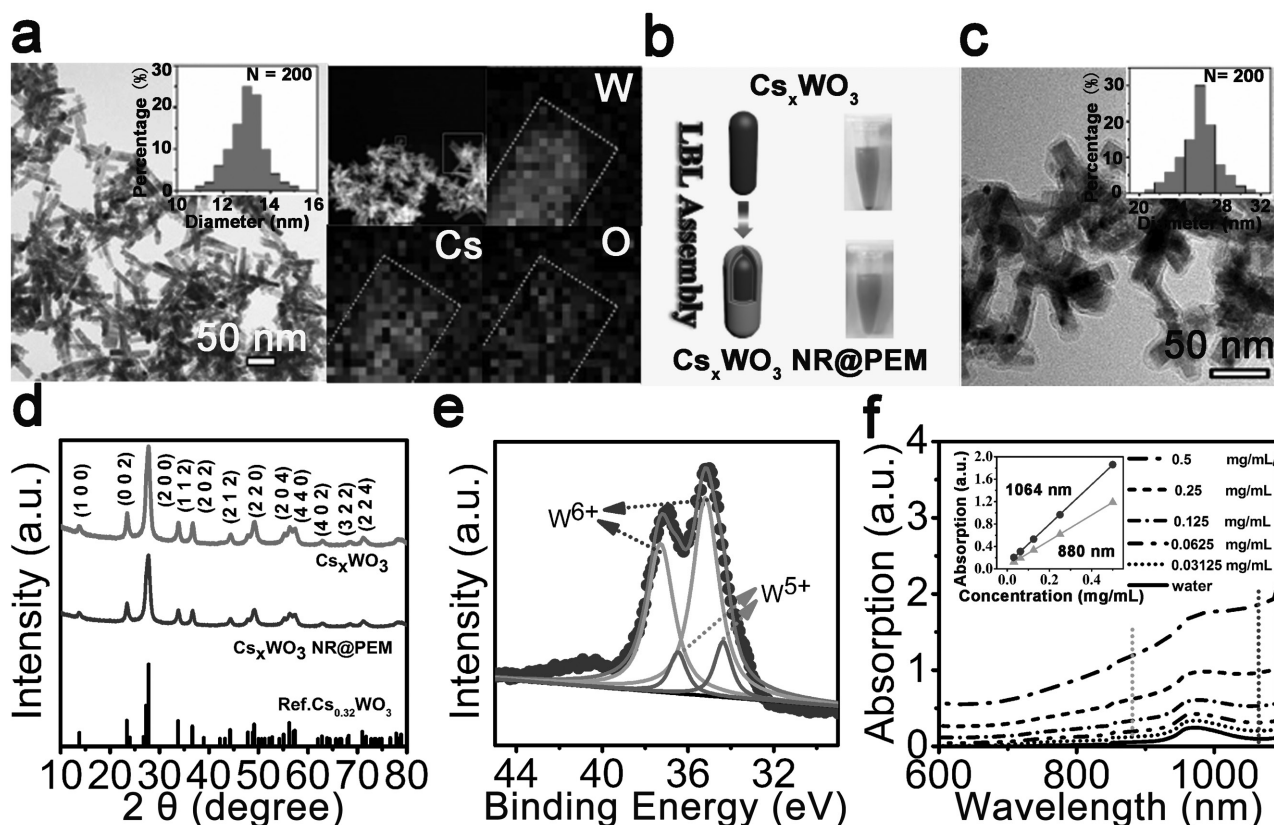© 2016 WILEY-VCH Verlag GmbH & Co. KGaA, Weinheim

Figure 1. a) TEM image and EDS mapping images of Cs$_x$WO$_3$ NRs. The inset shows size distribution of Cs$_x$WO$_3$ NR. b) Scheme of surface modification on Cs$_x$WO$_3$ NRs and photograph of Cs$_x$WO$_3$ NRs and Cs$_x$WO$_3$ NR@PEMs dispersed in culture medium containing 10% fetal bovine serum (v/v). c) TEM image of Cs$_x$WO$_3$ NR@PEM. The inset shows the size distribution of Cs$_x$WO$_3$ NR@PEM. d) XRD patterns of Cs$_x$WO$_3$ NRs and Cs$_x$WO$_3$ NR@PEMs (JCPDS No. 831334 shown as reference). e) Fitted XPS spectra on W 4f core level of Cs$_x$WO$_3$ NR@PEM. f) Absorption spectra of Cs$_x$WO$_3$ NR@PEM aqueous suspensions with different concentrations and corresponding linear fit between concentration and absorbance (inset: the top curve represents absorption intensity at 1064 nm and the bottom curve represents absorption intensity at 880 nm).

blood vessel heat sinks. Therefore, incorporating PD and PT therapy would create a synergy with improved treatment outcome.[15] Altogether, our work offers the unique opportunity for using one species for multimodal cancer imaging and therapy.

The Cs$_x$WO$_3$ NRs were first synthesized via a previously reported solvothermal method.[16] As shown in **Figure 1**a, as-prepared Cs$_x$WO$_3$ products exhibit rod-like morphology and uniform particle size. The diameter of these NRs is 13 ± 2 nm, while the length reaches 70 ± 5 nm. The chemical composition of NRs was then investigated by energy dispersive X-ray spectroscopy (EDS) and X-ray diffractometer (XRD). EDS mapping clearly indicates existence of Cs, W, and O elements in the NRs and the atomic of Cs/W is determined to be 0.32, being consistent with the expected phase of Cs$_{0.32}$WO$_3$ (Figure 1a and Figure S1, Supporting Information). The XRD pattern suggests the hexagonal structure of Cs$_{0.32}$WO$_3$ (JCPDS No. 831334), and no impurity peaks are detected (the curve in Figure 1d). As-prepared Cs$_x$WO$_3$ NRs are found to be well dispersed in water in virtue of their high zeta-potential value of −67.55 ± 0.92 mV; however, they spontaneously aggregate in the culture medium likely due to the compression of surface electric double layer. To improve the dispersibility of Cs$_x$WO$_3$ NRs in the culture medium, the surface of negative charged Cs$_x$WO$_3$ NRs was thus coated with polyelectrolyte multilayers via LBL assembly (Figure 1b). The

Cs$_x$WO$_3$ NRs were alternatively dispersed in solutions of positively charged polyallylamine hydrochloride (PAH) and negatively charged polystyrenesulfonate (PSS) for 10 min, followed by centrifuged and rinsed with 0.1 M NaCl solution to remove the excessive polyelectrolytes, and finally leading to formation of a Cs$_x$WO$_3$ NR@PAH/PSS/PAH structure (abbreviated as Cs$_x$WO$_3$ NR@PEM). As shown in Figure S2 in the Supporting Information, an alternative negative and positive zeta-potential as the PAH and PSS coating reveals successful modification of Cs$_x$WO$_3$ NRs with polyelectrolyte multilayers and the LBL assembly process of Cs$_x$WO$_3$ NRs involved in electrostatic interactions. Considering that a positively charged particle is more easily to be endocytosed by negatively charged cancer cells, the final outer layer of the modified NRs is designed as PAH so that the Cs$_x$WO$_3$ NR@PEM has positively charged surfaces. After surface modification, the obtained Cs$_x$WO$_3$ NR@PEM displays excellent dispersibility in culture medium containing 10% fetal bovine serum (v/v), and no obviously macroscopic aggregates are discerned even after 24 h storage (Figure 1b, inset). UV–vis–NIR spectroscopy and transmission electron microscopy (TEM) measurements confirm good stability of Cs$_x$WO$_3$ NR@PEM in phosphate buffered saline (PBS) and serum solution (Figure S3, Supporting Information). After coating with LBL polyelectrolyte multilayers, the diameter and length of Cs$_x$WO$_3$ NR increase

**ADVANCED
SCIENCE NEWS**

www.advancedsciencenews.com

**ADVANCED
MATERIALS**

www.advmat.de

COMMUNICATION

to 26 ± 5 and 85 ± 6 nm, respectively, as shown in Figure 1c, respectively. Dynamic light scattering (DLS) data also show that the hydrodynamic size of Cs_xWO_3 NRs increases from 122 ± 9 to 361 ± 4 nm after LBL modification (Figure S4, Supporting Information). Based on the TEM observations (Figure 1a,c), the thickness of PAH/PSS/PAH layers on Cs_xWO_3 NR surfaces is estimated to be ≈7 nm, and quantitative measurement by thermogravimetric analysis further manifests that there are around 11.4 wt% polyelectrolytes in Cs_xWO_3 NR@PEM (Figure S5, Supporting Information). Both TEM and DLS results confirm that the prepared Cs_xWO_3 NR and Cs_xWO_3 NR@PEM have uniform particle size. The larger hydrodynamic size of Cs_xWO_3 NR@PEM observed with DLS should be attributed to polyelectrolyte because the diameter of polyelectrolyte chains in solution typically is 20–100 nm.[17] Furthermore, this modification process has no impact on crystallinity and chemical valence of the sample, as confirmed by TEM image (Figure 1c), XRD data (Figure 1d), and X-ray photoelectron spectroscopy (XPS) (Figure 1e). Detailed investigation of XPS peaks corresponding to tungsten shows the mixed bonding state of tungsten element (Figure 1e). The main peaks with a W 4f 5/2 at 37.3 eV and a W 4f 7/2 at 35.2 eV are attributed to the W atoms with a chemical valence of +6, while the second doublet with a lower binding energy at 34.4 and 36.5 eV is assigned to the W 4f 5/2 and W 4f 7/2 core levels from W^{+5}. This mixed chemical

valence of W^{+5} and W^{+6} is in accordance with the typical characteristics of Cs_xWO_3 tungsten bronze, which can also be expressed as $Cs_xW_x^{+5}W_{1-x}^{+6}O_3$.[18] As demonstrated in the UV–vis–NIR absorption spectra (Figure 1f and Figure S3c and S6, Supporting Information), Cs_xWO_3 NR@PEM exhibits concentration-dependent absorbance increase in the whole NIR range of 780–2500 nm, fully embracing the desired biological windows I (650–950 nm)/II (1000–1350 nm). The NIR absorption feature of Cs_xWO_3 NR@PEM originates from its LSPR since tungsten bronze is a n-type semiconductor with relatively high concentration of free electrons as a result of Cs-doping,[19] whereby metalloid behavior appears. Because water has no absorption at 880 and 1064 nm (black curve in Figure 1f), we use 880 and 1064 nm laser for PAT and PT. The optical density at 880 and 1064 nm has a good linear relationship with concentration of Cs_xWO_3 NR@PEM (the inset of Figure 1f).

Given the wide and strong light absorption of Cs_xWO_3 NR@PEMs, the laser-induced heat generation of the aqueous suspensions of Cs_xWO_3 NR@PEMs was evaluated. 1 mL aqueous solution containing Cs_xWO_3 NR@PEM at various concentrations (0, 0.0625, 0.125, 0.25, and 0.5 mg mL^{-1}) was placed into the agar-phantom container and irradiated by two NIR lasers (880 or 1064 nm), respectively, at same power density of 2 W cm^{-2}. The temperature increase was tracked using a thermographic camera. As shown in **Figure 2**a,b, under 880 or
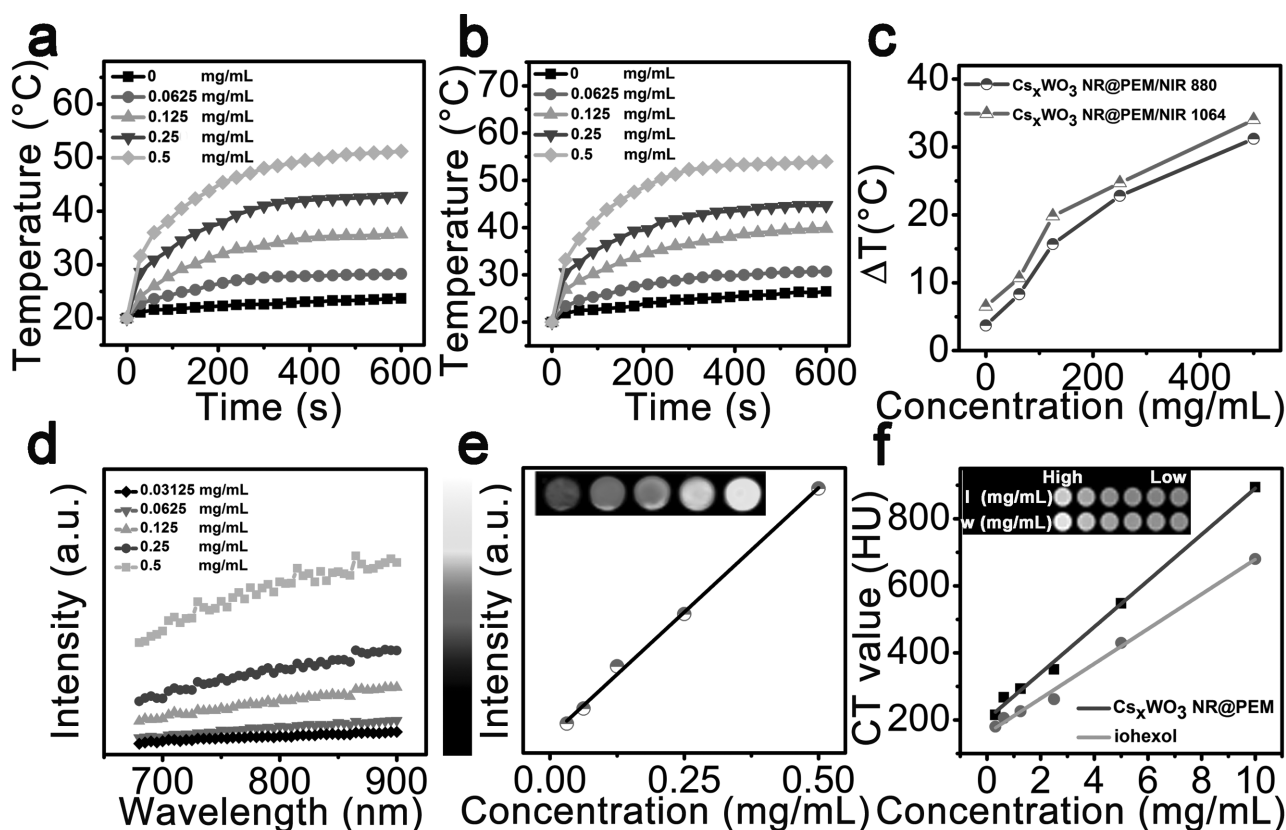

Figure 2. a,b) NIR-laser-induced heat generation of Cs_xWO_3 NR@PEM aqueous solution (power density of 2 W cm^{-2}): a) 880 nm and b) 1064 nm. c) Plot of temperature change (ΔT) over a period of 10 min irradiation versus Cs_xWO_3 NR@PEM concentration. d) PAT signal of Cs_xWO_3 NR@PEM solutions at different concentrations. e) PAT signal of Cs_xWO_3 NR@PEM as a function of concentration under 880 nm excitation (inset: in vitro PAT images of Cs_xWO_3 NR@PEM dispersed in distilled water with different concentrations). f) HU values of Cs_xWO_3 NR@PEM and commercial iohexol as function of the sample concentration (inset: in vitro CT images of Cs_xWO_3 NR@PEM (top line) and commercial iohexol (bottom line) dispersed in saline at different concentrations).

1064 nm irradiation, the temperature of all the Cs_xWO_3 NR@PEM dispersions increases rapidly at the beginning and then starts to level off after 5 min. The concentration-dependent temperature increase (Figure 2c) manifests that the Cs_xWO_3 NR@PEM could rapidly and efficiently convert the laser energy into local hyperthermia under both 880 and 1064 nm irradiation. We further compare the heating effect of an 880 nm and a 1064 nm continuous-wave laser on Cs_xWO_3 NR@PEM. It is noteworthy that, at each concentration, the temperature increment under 1064 nm irradiation is larger than that under 880 nm irradiation (Figure 2c), which should be attributed to higher absorbance intensity of the Cs_xWO_3 NR@PEM at 1064 nm (Figure 1f). The strong optical absorbance in the NIR region and remarkable light-heat conversion ability suggest that Cs_xWO_3 NR@PEM would be excellent agents for PAT and PT. The enhanced PAT effect of Cs_xWO_3 NR@PEM at various concentration is then examined in Figure 2d. PAT signal becomes stronger in the longer wavelength region, being consistent with tendency of optical absorption intensity of Cs_xWO_3 NR@PEM (Figure 1f). The higher absorbance endows higher thermoelastic expansion and thus stronger ultrasonic emission. Moreover, the PAT signal intensity is linearly correlated with the Cs_xWO_3 NR@PEM concentration under 880 nm laser excitation (Figure 2e). Another intriguing property of Cs_xWO_3 NR@PEM results from high atomic number element W (its atomic number is 73), which makes it be useful as CT contrast agent.[6,8] Therefore, we explored their enhanced CT effect. Figure 2f presents the CT image and Hounsfield unit (HU) values of Cs_xWO_3 NR@PEM at different concentrations, which shows a linear signal enhancement along with Cs_xWO_3 NR@PEM concentration increase. Impressively, the slope of HU value for Cs_xWO_3 NR@PEM is up to 68.84 HU L g^{-1} (top curve in Figure 2f), 1.33 times that of commercial CT contrast agent iohexol (51.84 HU L g^{-1}) (bottom curve in Figure 2f).

We next assessed the cytotoxicity of Cs_xWO_3 NR@PEM on several types of cells. The standard methyl thiazolyl tetrazolium (MTT) assay was carried out to determine the relative viabilities of one cancer cell line and two normal cells lines: HeLa (human epithelial carcinoma cancer cells), human umbilical vein endothelial normal cells, and human L02 (hepatic normal cells), after they were incubated with either Cs_xWO_3 NRs or Cs_xWO_3 NR@PEM at various concentrations for 24 h. As shown in Figure S7 in the Supporting Information, no obvious cytotoxicity of three types of cell lines is distinguished with treatment of either Cs_xWO_3 NRs or Cs_xWO_3 NR@PEM in a wide concentration range of 15.625–1000 µg mL^{-1}. Moreover, Cs_xWO_3 NR@PEM exhibits even lower cytotoxicity, indicating that surface modification of Cs_xWO_3 with polyelectrolytes could improve its biocompatibility. The above results suggest that both Cs_xWO_3 NRs and Cs_xWO_3 NR@PEM can serve as promising biocompatible probes for CT and PAT imaging and PT therapy.

To evaluate the potential capacity of Cs_xWO_3 NR@PEM for CT enhancement, Balb/c mice bearing HeLa tumors were intratumorally injected with Cs_xWO_3 NR@PEM dispersed in saline (4 mg mL^{-1}, 50 µL) or iohexol (3.73 mg mL^{-1}, 50 µL) and then imaged by quantum GX micro-CT-imaging system (**Figure 3**a and Figure S8, Supporting Information). After 5 min post-injection of Cs_xWO_3 NR@PEM, the CT signal

at tumor site is boosted, as marked by the red dashed circles (Figure 3a), with the HU value dramatically increasing from 278.5 ± 35.4 HU before injection to 606.6 ± 47.2 HU after injection. As for the mouse injected with iohexol, there are no clear tumor signals to be observed in CT images (Figure S8, Supporting Information), with the HU value slightly increasing from 286.3 ± 39.3 HU before injection to 305.1 ± 41.2 HU after injection, owing to its poor retention at tumor site.[20] These results prove that the Cs_xWO_3 NR@PEM is promising CT contrast agents for CT imaging of tumors.

The in vivo PAT imaging efficacy of Cs_xWO_3 NR@PEM is also examined (Figure 3b). The HeLa-tumor-bearing mice were intratumorally injected with 50 µL of Cs_xWO_3 NR@PEM (2 mg mL^{-1}) and the cross-sectional PAT images of the mice were obtained at different time intervals after injection (Figure 3b). It is evident that PAT signal intensity in tumor remarkably increases over time. In the control group injected with only PBS, the PAT signals remain unchanged. The in vivo experimental result indicates that Cs_xWO_3 NR@PEM is applicable contrast agents for PAT imaging in vivo. Taken together, above results suggest that our Cs_xWO_3 NR@PEM system possesses excellent PAT and CT imaging capability and is able to depict tumor or deep tissue.

Encouraged by the strong optical absorbance in the NIR region and remarkable light-heat conversion ability of Cs_xWO_3 NR@PEM, we then investigated in vitro PT effect of Cs_xWO_3 NR@PEM on HeLa cells. The live/dead double-staining method was used to evaluate the laser-triggered PT effect of Cs_xWO_3 NR@PEM: Calcein AM stained the live cells with green emission whereas propidium iodide (PI) dye stained the dead cells with red emission. Evidently, no red color is seen in control (**Figure 4**a), Cs_xWO_3 NR@PEM only (Figure 4b), and laser only (Figure 4c,d) groups. On the contrary, in the Cs_xWO_3 NR@PEM/NIR (880 or 1064 nm) laser group, a significant amount of cellular deaths are observed, as indicated by the red fluorescence within the laser irradiation spot, and the area of the dead cell cycle enlarges dramatically with prolonged irradiation duration (Figure 4e,f), indicating the superior PT potency of Cs_xWO_3 NR@PEM against HeLa cells.

It was reported that photogenerated electrons of oxygen-deficient tungsten oxides such as $W_{18}O_{49}$ could react with the absorbed O_2 to generate reactive oxygen species (ROS, including singlet oxygen and $\cdot O_2^-$)[10b,21] and thus act as PD therapy photosensitizer for killing cancer cells and destructing solid tumors. To clarify whether Cs_xWO_3 NR@PEM on HeLa cells get a good PD effect, we investigated the capability of Cs_xWO_3 NR@PEM to sensitize the formation of ROS upon photoexcitation using the 1,3-diphenylisobenzofuran (DPBF)-based spectroscopic method. The DPBF probe reacts with the singlet oxygen $^1O_2$ to be decomposed into 1,2-dibenzoylbenzene, thus leading to a decrease in optical absorption intensity at 410 nm.[22] **Figure 5**a summarizes the UV–vis absorption spectra of DPBF solution containing 1 mg mL^{-1} Cs_xWO_3 NR@PEM upon illumination with 880 or 1064 nm laser (2 W cm^{-2}). Obviously, the optical absorption values at 410 nm significantly decrease with prolonged irradiation duration (green and blue curves in Figure 5a). The formation of singlet oxygen was also monitored by X-band electron spin resonance (ESR) with the spin traps 2,2,6,6-tetramethyl-4-piperidone (TEMP). As
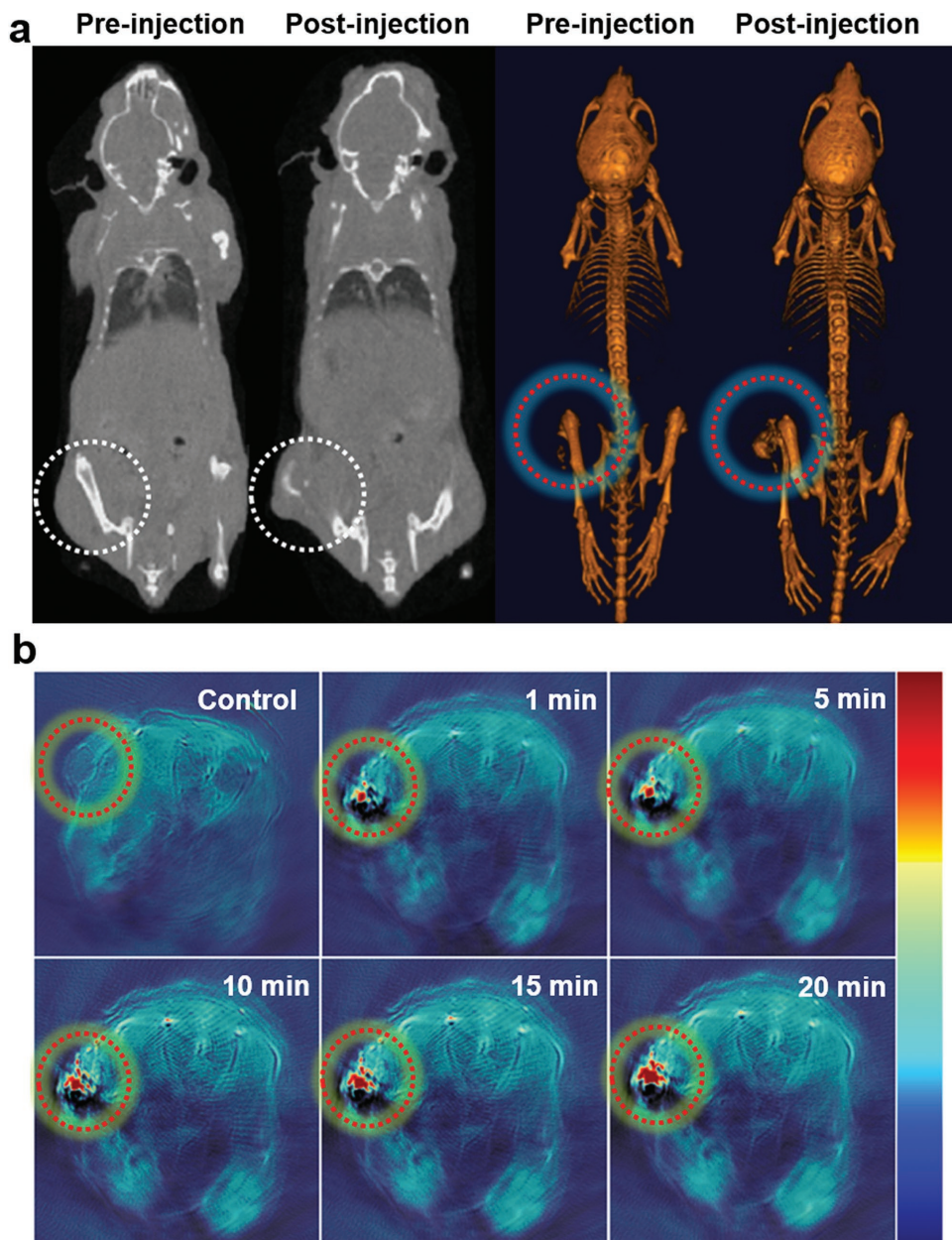
ADVANCED
SCIENCE NEWS
www.advancedsciencenews.com

ADVANCED
MATERIALS
www.advmat.de

COMMUNICATION

Figure 3. In vivo CT and PAT imaging. a) CT images of mice before and after intratumoral injection with Cs_xWO_3 NR@PEM dispersed in saline (4 mg mL^{-1}, 50 μL). The CT contrast is obviously enhanced in the mouse tumor (red dashed circles). b) In vivo PAT images of HeLa-tumor-bearing mice before and after intratumoral injection of 50 μL of Cs_xWO_3 NR@PEM (2 mg mL^{-1}) for different times. Tumor sites are marked with red dashed circles.

displayed by green and blue curves in Figure 5b, when the mixture of Cs_xWO_3 NR@PEM and TEMP probes is illuminated with 880 or 1064 nm laser (2 W cm^{-2}) at room temperature, a typical three lines ESR signal with equal intensity (a^N = 16.3 G, g = 2.0056) is recorded, which is assigned to 2,2,6,6-tetramethyl-1-piperidinyloxy (TEMPO),[23] a stable nitroxide radical generated from TEMP and $^1O_2$. Finally, the intracellular generation of ROS in Cs_xWO_3 NR@PEM-internalized HeLa cells after NIR light irradiation is investigated (Figure 5c). The HeLa cells incubated with H_2O_2 (50 × 10^{-3} M) are used as positive control. Visualization of intracellular generation of singlet oxygen is realized by a probe of 2′,7′-dichlorofluorescin diacetate (H_2DCFDA), which

is a cell-permeable nonfluorescent molecule and can turn to highly fluorescent 2′,7′-dichloroflorescein with green emission upon reaction with singlet oxygen. As seen in Figure 5c, a strong green fluorescence is observed both in the H_2O_2 positive control and the Cs_xWO_3 NR@PEM/NIR (880 or 1064 nm) laser groups, whereas almost no discriminable fluorescence is discerned in the negative control group and the laser-only groups. These data confirm that photoirradiation of Cs_xWO_3 NR@PEM can generate singlet oxygen under either 880 or 1064 nm NIR irradiation and act as NIR-light-activatable PD reagents at the cellular level.

Figure 5d shows that irradiation of Cs_xWO_3 NR@PEM-internalized HeLa cells with 880 or 1064 nm (2 W cm^{-2}) both lead to
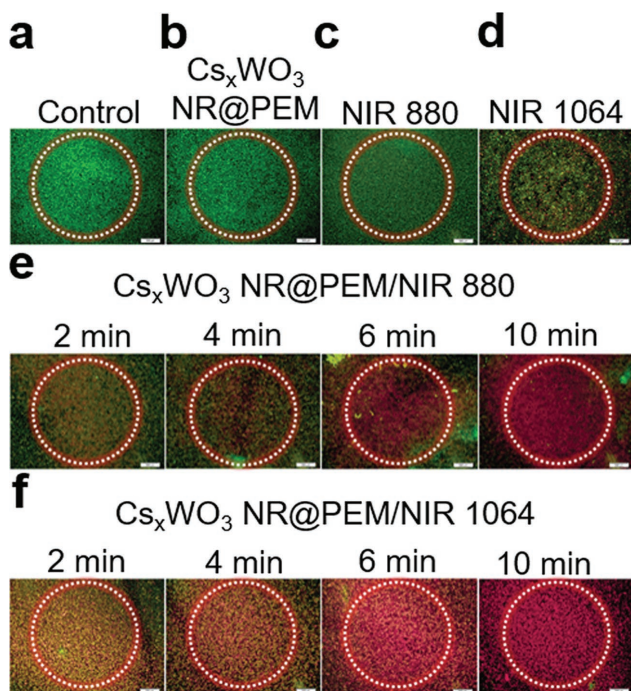
COMMUNICATION

Figure 4. In vitro PT/PD therapy effect of Cs$_x$WO$_3$ NR@PEMs against HeLa cells. a–f) Fluorescence images of Calcein AM (live cells, green fluorescence) and PI (dead cells, red fluorescence) co-stained HeLa cells incubated with Cs$_x$WO$_3$ NR@PEM (250 µg mL^{-1}) for 24 h after laser irradiation.

a significant amount of cellular deaths (over 90%), which should be caused by the combined NIR-light-activatable PD and PT effect. In order to differentiate the PD effect from the PT effect, Cs$_x$WO$_3$ NR@PEM-internalized HeLa cells were irradiated with an 880 nm or a 1064 nm laser (2 W cm^{-2}) in the temperature chamber at 4 °C, so the temperature of the irradiation area never exceeded 10 °C (Figure S9, Supporting Information) and the light-irradiation-induced photothermal ablation was almost entirely suppressed. As shown in Figure 5d, the cell-inhibition rates are just 30.6% for 880 nm and 35.5% for 1064 nm. To further seek the supporting evidence for the PT effect of Cs$_x$WO$_3$ NR@PEM, the cell viability under 880 or 1064 nm light irradiation was measured with Cs$_x$WO$_3$ NR@PEM-uptaken HeLa cells preincubated with sodium azide (NaN$_3$), a well-known singlet-oxygen quencher.[14b] The presence of NaN$_3$ suppresses the generation of singlet oxygen and thus eliminates the PD effect. As displayed in Figure 5d, cellular inhibition rates are 60.3% for 880 nm and 65.8% for 1064 nm. Based on the above results, we conclude that the PT effect induced by Cs$_x$WO$_3$ NR@PEM is considerably larger than the PD effect. All these results clearly reveal that the working mechanism involved in the photodestruction of cancer cells using Cs$_x$WO$_3$ NR@PEM is composed of Cs$_x$WO$_3$ NR@PEM-mediated singlet-oxygen-induced cellular deaths (i.e., PD effect) and Cs$_x$WO$_3$ NR@PEM-induced hyperthermia effect.

Motivated by in vitro therapeutic effect, we further carried out in vivo experiments to evaluate the treatment efficiency of HeLa tumors in mice by using Cs$_x$WO$_3$ NR@PEM. After being intratumorally injected with 100 µL PBS or 1 mg mL^{-1} Cs$_x$WO$_3$

NR@PEM, HeLa-tumor-bearing nude mice were exposed to an 880 nm or a 1064 nm laser with a power density of 2 W cm^{-2}. First, the surface temperature of the tumor site under NIR laser irradiation was monitored using an IR thermal camera. As indicated in **Figure 6**a,b, photoirradiation of Cs$_x$WO$_3$ NR@PEM-injected mice for 10 min results in significant elevation of local temperature from 37.0 to 54.2 °C by 880 nm or 56.8 °C by 1064 nm, whereas a slight temperature increase is observed for Cs$_x$WO$_3$ NR@PEM-free PBS-injected mice under the same conditions. Extension of the irradiation time could further increase the local temperature. It is known that cancer cells are less tolerant to the hyperthermia effect than healthy cells because tissue overgrowth limits the heat dissipation from the tumor, especially at such temperatures higher than 48 °C, over which irreversible damage would happen within short exposure (4–6 min).[24] Subsequently, we evaluated the in vivo phototherapeutic effect of Cs$_x$WO$_3$ NR@PEM using a HeLa-tumor-bearing mice model. When the tumor size reached about 400–500 mm^3, the tumor-bearing nude mice were randomly divided into eight groups: a control group, a Cs$_x$WO$_3$ NR@PEM group, an 880 nm laser group, a 1064 nm laser group, a group for Cs$_x$WO$_3$ NR@PEM plus 880 nm laser irradiation for 5 min, a group for Cs$_x$WO$_3$ NR@PEM plus 880 nm laser irradiation for 10 min, a group for Cs$_x$WO$_3$ NR@PEM plus 1064 nm laser irradiation for 5 min, and a group for Cs$_x$WO$_3$ NR@PEM plus 1064 nm laser irradiation for 10 min. Each group contained five mice. The absorbances of the injected Cs$_x$WO$_3$ NR@PEM were 2.322 and 3.620 at 880 and 1064 nm, respectively. The tumor volume change was quantitatively monitored over time for evaluating the in vivo anticancer efficacy. As demonstrated in Figure 6c, the tumors in control group (black curve), Cs$_x$WO$_3$ NR@PEM group (red curve), 880 nm laser group (green curve), and 1064 nm laser group (blue curve) keep growing, indicating that Cs$_x$WO$_3$ NR@PEM itself could not effectively inhibit the tumor growth in absence of NIR irradiation, which is also another piece of evidence to prove the excellent biocompatibility of Cs$_x$WO$_3$ NR@PEM and in accordance with previous MTT results (Figure S7, Supporting Information).

By comparing the growth speed of the tumors in control group, Cs$_x$WO$_3$ NR@PEM group, 880 nm laser group, and 1064 nm laser group, one can find that 880 or 1064 nm laser irradiation (green or blue curve in Figure 6c) gives rise to slower tumor-growth speed, possibly due to heat effect induced by 880 or 1064 nm laser irradiation that might stimulate the immune effect.[14b] Interestingly enough, the sizes of HeLa tumors on mice treated with Cs$_x$WO$_3$ NR@PEM strongly depend on irradiation duration. Regardless of adopting 880 or 1064 nm laser, the treatment is effective at early stage for the Cs$_x$WO$_3$ NR@PEM-injected groups that receive 5 min laser irradiation, but recurrence of tumors growth happens after first week (cyan or magenta curve in Figure 6c), indicating that the short-time phototherapy is not sufficient for complete tumor elimination. When the irradiation time extends to 10 min, complete tumor elimination is achieved in the Cs$_x$WO$_3$ NR@PEM-injected groups. Note that the body weights of mice for all eight groups do not show any noticeable change or difference during the course of therapy (Figure 6d), also implying that the proposed system in this work has no acute toxicity.
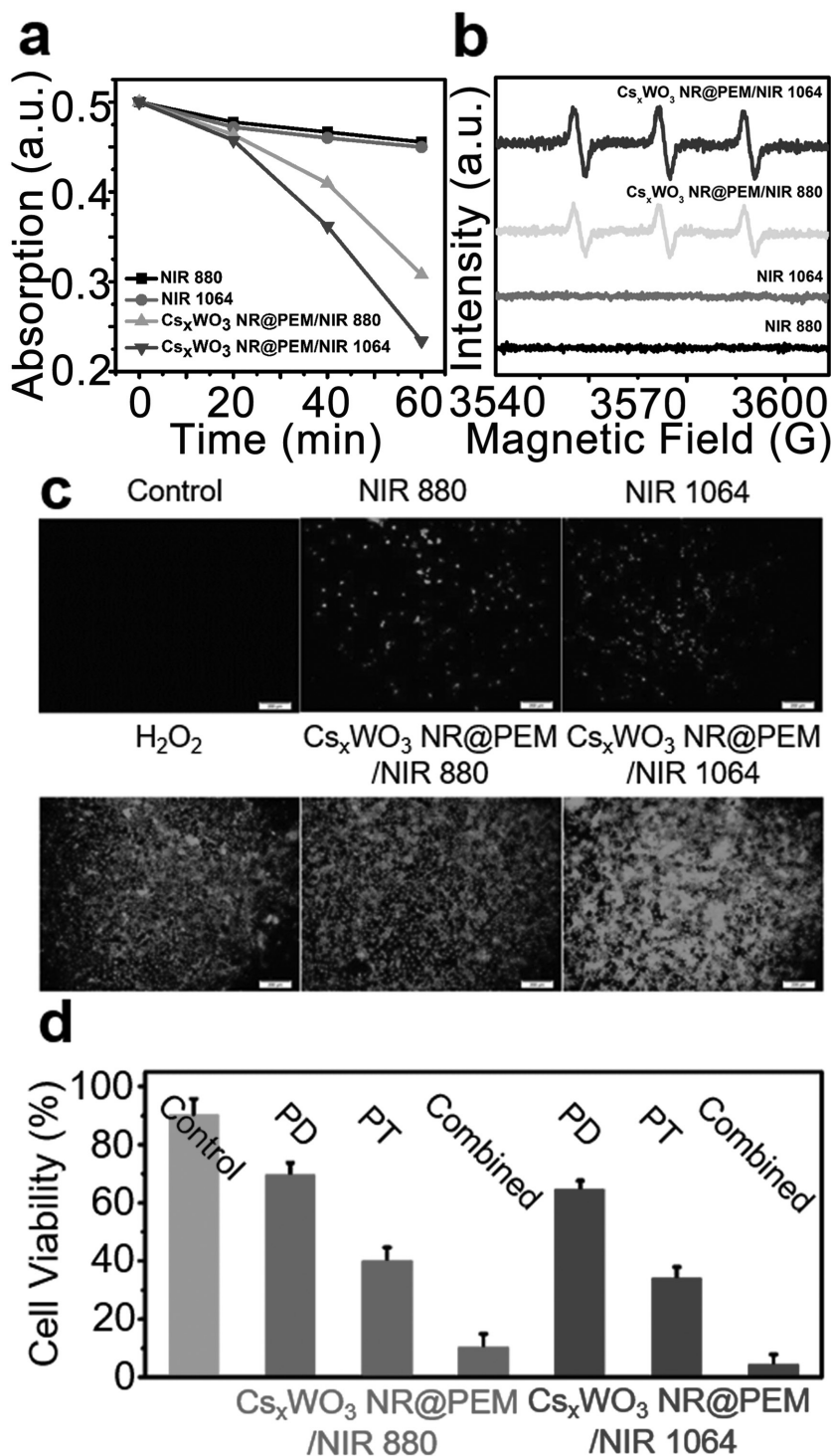
ADVANCED
SCIENCE NEWS

www.advancedsciencenews.com

ADVANCED
MATERIALS

www.advmat.de

COMMUNICATION

Figure 5. Detection of singlet oxygen production by NIR light triggered Cs_xWO_3 NR@PEM. a) Absorption spectra of Cs_xWO_3 NR@PEM solution after adding DPBF probes under different irradiation times. b) ESR spectra of Cs_xWO_3 NR@PEM with TEMP probes under 10 min irradiation. c) Fluorescence images of ROS generation in HeLa cells incubated with Cs_xWO_3 NR@PEM (250 µg mL^{-1}) for 24 h after laser irradiation (NIR laser: 2 W cm^{-2}, 10 min; green emission from ROS indicator H_2DCFDA; scale bar, 200 µm). d) Relative cell viability of HeLa after different treatments (only PD groups, only PT groups and PD/PT combined groups) with Cs_xWO_3 NR@PEM (250 µg mL^{-1}) for 24 h incubation (irradiation time: 10 min).

After PT/PD treatment, the mice show the black scars at their original sites of tumor (Figure 6e and Figure S10, Supporting Information). To provide a deep insight into the mechanism of tumor-growth inhibition and examine the potential toxicity of Cs_xWO_3 NR@PEM in vivo, the mice were sacrificed 14 d later after phototherapy and histology analysis of tumor tissues was performed via a typical hematoxylin and eosin (H&E) method. As indicated in Figure 6f, H&E staining of tumor slices reveals that the tumor cells after the combined PT/PD therapy are severely damaged as evidenced by severe cell necrosis and apoptosis, especially for the group with longer therapeutic duration (red and blue arrows); while negligible damage is found in other control groups. Such histology analysis highlights the excellent phototherapeutic efficacy induced by the combined PD/PT treatment. Notably, H&E staining of the main organs including the liver, kidney, heart, lung, and spleen from different groups of mice displays no detectable lesions, such as necrosis, hydropic degeneration, inflammatory, pulmonary fibrosis in the sections of tissues (Figure S11, Supporting Information), suggesting that the Cs_xWO_3 NR@PEM system is a type of in vivo biocompatible agents for cancer treatment.

Finally, in order to understand the possible metabolic pathway of Cs_xWO_3 NR@PEM, we measured the comparative tissue distribution of Cs_xWO_3 NR@PEM. After a single intravenous dose of 100 µL of 1 mg mL^{-1} Cs_xWO_3 NR@PEM, the W level in the tumor and the major organs was measured by inductively coupled plasma mass spectrometry (ICP-MS). As demonstrated in Figure S12 in the Supporting Information, both the liver and the tumor show the highest W concentration at 24 h. The maximum concentration of W occurring in the tumors confirms that Cs_xWO_3 NR@PEM can passively target the tumors through enhanced permeability and retention (EPR) effects. The higher W level in the liver is because the reticuloendothelial system would filter Cs_xWO_3 NR@PEM from the bloodstream. After 14 d, the W level in all investigated tissues decreases and follows the order of: liver > kidney ≈ lung > spleen> tumor > heart. The maximum concentration of W occurring in the liver suggests that Cs_xWO_3 NR@PEM could be mainly cleared by liver. Previous studies have indicated that the liver is the most effective elimination pathway for nanoparticles because fenestrated sinusoids in liver blood vessels have average pore sizes of 100–200 nm and
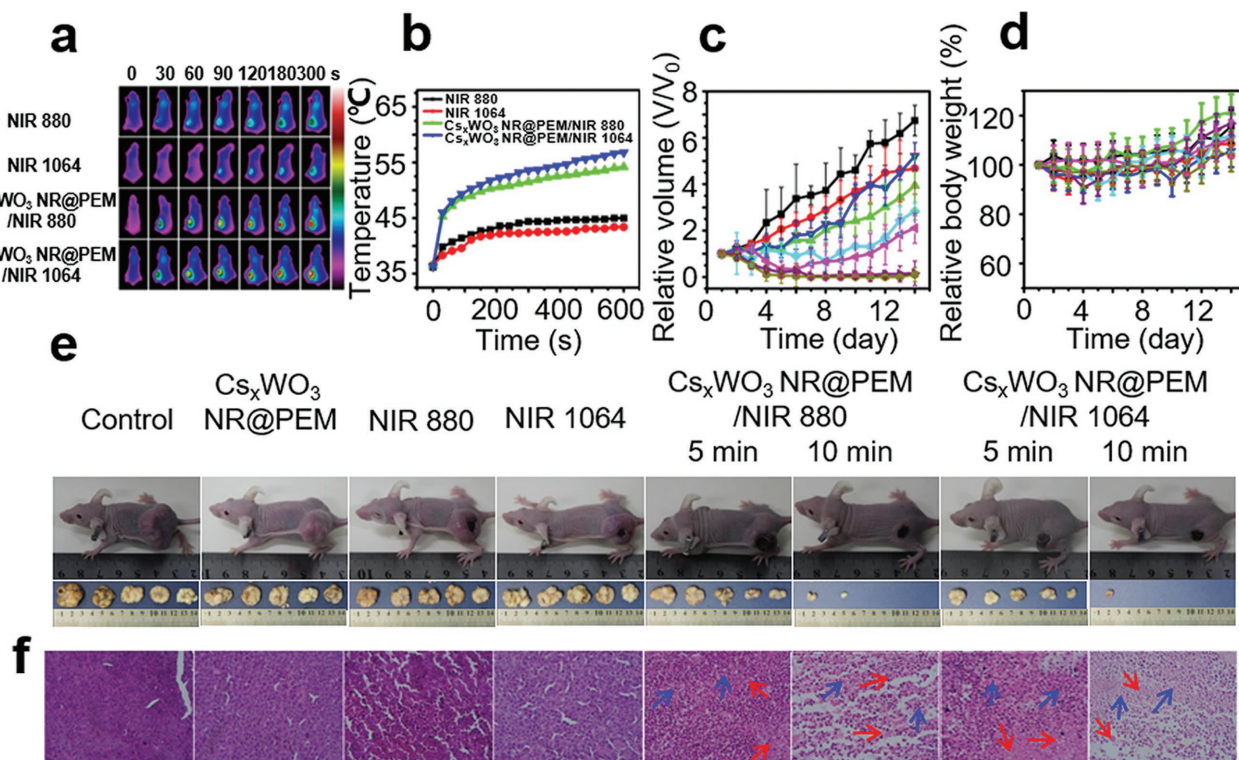
COMMUNICATION

Figure 6. In vivo PT/PD therapy. a) Infrared thermal images of HeLa-tumor-bearing mice after injected with Cs_xWO_3 NR@PEM under 880 or 1064 nm NIR laser radiation. The absorbance of the injected Cs_xWO_3 NR@PEM is 2.322 and 3.620 at 880 and 1064 nm, respectively. b) Temperature variation of tumors monitored by the IR thermal camera on different groups during laser irradiation. c,d) Quantitative measurement of tumor volume in mice and body weight of mice at different points after various treatment (black: control, red: only Cs_xWO_3 NR@PEM, green: NIR 880, blue: NIR 1064, cyan: Cs_xWO_3 NR@PEM/NIR 880 nm 5 min, magenta: Cs_xWO_3 NR@PEM/NIR 1064 nm 5 min, purple: Cs_xWO_3 NR@PEM/NIR 880 nm 10 min, dark yellow: Cs_xWO_3 NR@PEM/NIR 1064 nm 10 min). e) Representative photos of HeLa-tumor-bearing mice and tumors after 14 d treatment. f) Histology staining of tumor slices collected from different groups of mice after 14 d treatment (red arrow: necrocytosis; blue arrow: apoptosis).

can filter the nanoparticles or line with the Kupffer cells to quickly phagocytize the nanoparticles.[25a] The higher W lever in the kidney and spleen is attributed to the nephrons of kidney and reticular meshwork of spleen, which can also selectively filter the nanoparticles from the blood to a certain extent.[25b,c]

In summary, we have developed a Cs_xWO_3-based "four-in-one" multifunctional theranostic agent for CT/PAT dual-imaging-guided PT/PD cancer dual therapy. The Cs_xWO_3 NR@PEM system has strong light absorption in the NIR region and exhibits excellent biocompatibility toward both malignant HeLa cells and normal cells. In vivo studies suggest Cs_xWO_3 NR@PEM as promising contrast agents for CT and PAT imaging on tumor or deep tissue. Furthermore, in vitro and in vivo investigations demonstrate its great superiority as novel photothermal and photodynamic agents for NIR-induced PT/PD ablation of cancer, as a result of their remarkable photothermal conversion efficiency as well as their great ability to sensitize formation of singlet oxygen. Impressively, under irradiation with 880 or 1064 nm laser (2 W cm^{-2}, 10 min), complete tumor ablation is successfully achieved in Cs_xWO_3 NR@PEM administrated group (5 mg kg^{-1} of Cs_xWO_3 NR@PEM). Importantly, during the experimental course, Cs_xWO_3 NR@PEM shows no evident toxicity toward major organs of treated mice. In virtue of complementary functions of CT (3D whole body) and PAT (high spatial resolution) imaging as well as PT (the inner part of tumors) and PD (the outer part of tumors) therapy, Cs_xWO_3 NR@PEM system will open the avenue toward development of the simple but general solutions for future bioimaging and cancer treatment.

Supporting Information

Supporting Information is available from the Wiley Online Library or from the author.

Acknowledgements

[1] a) J. Rieffel, U. Chitgupi, J. F. Lovell, *Small* **2015**, *11*, 4445; b) D. D. Wang, Z. Guo, J. J. Zhou, J. Chen, G. Z. Zhao, R. H. Chen, M. N. He, Z. B. Liu, H. B. Wang, Q. W. Chen, *Small* **2015**, *11*, 5956; c) H. W. Yang, H. L. Liu, M. L. Li, I. W. Hsi, C. T. Fan, C. Y. Huang, Y. J. Lu, M. Y. Hua, H. Y. Chou, J. W. Liaw, C. C. M. Ma, K. C. Wei, *Biomaterials* **2013**, *34*, 5651; d) H. Gong, Z. L. Dong, Y. M. Liu, S. N. Yin, L. Cheng, W. Y. Xi, J. Xiang, K. Liu, Y. G. Li, Z. Liu, *Adv. Funct. Mater.* **2014**, *24*, 6492; e) L. S. Lin, Z. X. Cong, J. B. Cao, K. M. Ke, Q. L. Peng, J. H. Gao, H. H. Yang, G. Liu, X. Y. Chen, *ACS Nano* **2014**, *8*, 3876; f) X. L. Sun, X. L. Huang, X. F. Yan, Y. Wang, J. X. Guo, O. Jacobson, D. B. Liu, L. P. Szajek, W. L. Zhu, G. Niu, D. O. Kiesewetter, S. H. Sun, X. Y. Chen, *ACS Nano* **2014**, *8*, 8438; g) M. Zhou, R. Zhang, M. A. Huang, W. Lu, S. L. Song, M. P. Melancon, M. Tian, D. Liang, C. Li, *J. Am. Chem. Soc.* **2010**, *132*, 15351; h) X. J. Wang, C. Wang, L. Cheng, S. T. Lee, Z. Liu, *J. Am. Chem. Soc.* **2012**, *134*, 7414; i) X. G. Ding, C. H. Liow, M. X. Zhang, R. J. Huang, C. Y. Li, H. Shen, M. Y. Liu, Y. Zou, N. Gao, Z. J. Zhang, Y. G. Li, Q. B. Wang, S. Z. Li, J. Jiang, *J. Am. Chem. Soc.* **2014**, *136*, 15684; j) R. C. Lv, C. N. Zhong, R. M. Li, P. P. Yang, F. He, S. L. Gai, Z. Y. Hou, G. X. Yang, J. Lin, *Chem. Mater.* **2015**, *27*, 1751; k) T. Liu, S. X. Shi, C. Liang, S. D. Shen, L. Cheng, C. Wang, X. J. Song, S. Goel, T. E. Barnhart, W. B. Cai, Z. Liu, *ACS Nano* **2015**, *9*, 950; l) P. Huang, J. Lin, W. W. Li, P. F. Rong, Z. Wang, S. J. Wang, X. P. Wang, X. L. Sun, M. Aronova, G. Niu, R. D. Leapman, Z. H. Nie, X. Y. Chen, *Angew. Chem., Int. Ed.* **2013**, *52*, 13958; m) S. Li, L. G. Xu, W. Ma, X. L. Wu, M. Z. Sun, H. Kuang, L. B. Wang, N. A. Kotov, C. L. Xu, *J. Am. Chem. Soc.* **2016**, *138*, 306; n) M. Z. Sun, L. G. Xu, W. Ma, X. L. Wu, H. Kuang, L. B. Wang, C. L. Xu, *Adv. Mater.* **2016**, *28*, 898; o) X. Zhao, L. Xu, M. Sun, W. Ma, X. Wu, H. Kuang, L. Wang, C. Xu, *Small* **2016**, *12*, 4662.

[2] Y. Yang, H. X. Wu, B. Z. Shi, L. L. Guo, Y. J. Zhang, X. An, H. Zhang, S. P. Yang, *Part. Part. Syst. Charact.* **2015**, *32*, 668.

[3] a) L. H. V. Wang, L. Gao, *Annu. Rev. Biomed. Eng.* **2014**, *16*, 155; b) L. H. Wang, D. Pile, *Nat. Photonics* **2011**, *5*, 183; c) G. Y. Chen, T. Y. Ohulchanskyy, S. Liu, W. C. Law, F. Wu, M. T. Swihart, P. N. Prasad, *ACS Nano* **2012**, *6*, 2969; d) L. M. Nie, X. Y. Chen, *Chem. Soc. Rev.* **2014**, *43*, 7132; e) L. M. Nie, S. J. Wang, X. Y. Wang, P. F. Rong, A. Bhirde, Y. Ma, G. Liu, P. Huang, G. M. Lu, X. Y. Chen, *Small* **2014**, *10*, 1585; f) Y. Liu, L. Nie, X. Chen, *Trends Biotechnol.* **2016**, *34*, 420; g) X. L. Liang, Y. Y. Li, X. D. Li, L. J. Jing, Z. J. Deng, X. L. Yue, C. H. Li, Z. F. Dai, *Adv. Funct. Mater.* **2015**, *25*, 1451; h) Y. M. Zhang, M. Jeon, L. J. Rich, H. Hong, J. M. Geng, Y. Zhang, S. X. Shi, T. E. Barnhart, P. Alexandridis, J. D. Huizinga, M. Seshadri, W. B. Cai, C. Kim, J. F. Lovell, *Nat. Nanotechnol.* **2014**, *9*, 631.

[4] M. Chen, S. H. Tang, Z. D. Guo, X. Y. Wang, S. G. Mo, X. Q. Huang, G. Liu, N. F. Zheng, *Adv. Mater.* **2014**, *26*, 8210.

[5] a) A. de la Zerda, S. Bodapati, R. Teed, S. Y. May, S. M. Tabakman, Z. Liu, B. T. Khuri-Yakub, X. Y. Chen, H. J. Dai, S. S. Gambhir, *ACS Nano* **2012**, *6*, 4694; b) M. Eghtedari, A. Oraevsky, J. A. Copland, N. A. Kotov, A. Conjusteau, M. Motamedi, *Nano Lett.* **2007**, *7*, 1914.

[6] a) K. L. Ai, Y. L. Liu, J. H. Liu, Q. H. Yuan, Y. Y. He, L. H. Lu, *Adv. Mater.* **2011**, *23*, 4886; b) J. H. Liu, J. G. Han, Z. C. Kang, R. Golamaully, N. N. Xu, H. P. Li, X. L. Han, *Nanoscale* **2014**, *6*, 5770.

[7] K. E. Dekrafft, Z. G. Xie, G. H. Cao, S. Tran, L. Q. Ma, O. Z. Zhou, W. B. Lin, *Angew. Chem., Int. Ed.* **2009**, *48*, 9901.

[8] L. Cheng, J. J. Liu, X. Gu, H. Gong, X. Z. Shi, T. Liu, C. Wang, X. Y. Wang, G. Liu, H. Y. Xing, W. B. Bu, B. Q. Sun, Z. Liu, *Adv. Mater.* **2014**, *26*, 1886.

[9] D. Huo, J. He, H. Li, A. J. Huang, H. Y. Zhao, Y. Ding, Z. Y. Zhou, Y. Hu, *Biomaterials* **2014**, *35*, 9155.

[10] a) Z. F. Huang, J. J. Song, L. Pan, X. W. Zhang, L. Wang, J. J. Zou, *Adv. Mater.* **2015**, *27*, 5309; b) P. Kalluru, R. Vankayala, C. S. Chiang, K. C. Hwang, *Angew. Chem., Int. Ed.* **2013**, *52*, 12332; c) Z. G. Chen, Q. Wang, H. L. Wang, L. S. Zhang, G. S. Song, L. L. Song, J. Q. Hu, H. Z. Wang, J. S. Liu, M. F. Zhu, D. Y. Zhao, *Adv. Mater.* **2013**, *25*, 2095.

[11] a) Z. G. Zhou, B. Kong, C. Yu, X. Y. Shi, M. W. Wang, W. Liu, Y. A. Sun, Y. J. Zhang, H. Yang, S. P. Yang, *Sci. Rep.* **2014**, *4*, 3653; b) J. H. Liu, J. G. Han, Z. C. Kang, R. Golamaully, N. N. Xu, H. P. Li, X. L. Han, *Nanoscale* **2014**, *6*, 5770.

[12] a) P. Vijayaraghavan, C. H. Liu, R. Vankayala, C. S. Chiang, K. C. Hwang, *Adv. Mater.* **2014**, *26*, 6689; b) S. Lal, S. E. Clare, N. J. Halas, *Acc. Chem. Res.* **2008**, *41*, 1842; c) R. Bardhan, S. Lal, A. Joshi, N. J. Halas, *Acc. Chem. Res.* **2011**, *44*, 936.

[13] K. H. Kim, R. G. Geronemus, *Dermatol. Surg.* **2006**, *32*, 241.

[14] a) V. Saxena, M. Sadoqi, J. Shao, *J. Pharm. Sci.* **2003**, *92*, 2090; b) W. S. Kuo, Y. T. Chang, K. C. Cho, K. C. Chiu, C. H. Lien, C. S. Yeh, S. J. Chen, *Biomaterials* **2012**, *33*, 3270; c) J. F. Lovell, C. S. Jin, E. Huynh, T. D. MacDonald, W. G. Cao, G. Zheng, *Angew. Chem., Int. Ed.* **2012**, *51*, 2429.

[15] a) B. Jang, J. Y. Park, C. H. Tung, I. H. Kim, Y. Choi, *ACS Nano* **2011**, *5*, 1086; b) J. Wang, G. Z. Zhu, M. X. You, E. Q. Song, M. I. Shukoor, K. J. Zhang, M. B. Altman, Y. Chen, Z. Zhu, C. Z. Huang, W. H. Tan, *ACS Nano* **2012**, *6*, 5070; c) L. Gao, J. B. Fei, J. Zhao, H. Li, Y. Cui, J. B. Li, *ACS Nano* **2012**, *6*, 8030; d) J. Lin, S. J. Wang, P. Huang, Z. Wang, S. H. Chen, G. Niu, W. W. Li, J. He, D. X. Cui, G. M. Lu, X. Y. Chen, Z. H. Nie, *ACS Nano* **2013**, *7*, 5320; e) C. S. Jin, J. F. Lovell, J. Chen, G. Zheng, *ACS Nano* **2013**, *7*, 2541.

[16] C. S. Guo, S. Yin, H. J. Yu, S. Q. Liu, Q. Dong, T. Goto, Z. W. Zhang, Y. P. Li, T. Sato, *Nanoscale* **2013**, *5*, 6469.

[17] I. Szilagyi, G. Trefalt, A. Tiraferri, P. Maroni, M. Borkovec, *Soft Matter* **2014**, *10*, 2479.

[18] C. S. Guo, S. Yin, M. Yan, T. Sato, *J. Mater. Chem.* **2011**, *21*, 5099.

[19] a) D. W. Lynch, R. Rosei, J. H. Weaver, C. G. Olson, *J. Solid State Chem.* **1973**, *3*, 242; b) J. Yan, T. Wang, G. Wu, W. Dai, N. Guan, L. Li, J. Gong, *Adv. Mater.* **2015**, *27*, 1580; c) K. Manthiram, A. P. Alivisatos, *J. Am. Chem. Soc.* **2012**, *134*, 3995; d) Y. Lu, Y. Jiang, X. Gao, X. Wang, W. Chen, *J. Am. Chem. Soc.* **2014**, *136*, 11687.

[20] C. Peng, L. F. Zheng, Q. Chen, M. W. Shen, R. Guo, H. Wang, X. Y. Cao, G. X. Zhang, X. Y. Shi, *Biomaterials* **2012**, *33*, 1107.

[21] a) Z. F. Huang, J. J. Zou, L. Pan, S. Wang, X. Zhang, L. Wang, *Appl. Catal., B* **2014**, *147*, 167; b) P. Kalluru, R. Vankayala, C. S. Chiang, K. C. Hwang, *Angew. Chem., Int. Ed.* **2013**, *52*, 12332.

[22] I. B. C. Matheson, J. Lee, B. S. Yamanashi, M. L. Wolbarsht, *J. Am. Chem. Soc.* **1974**, *96*, 3343.

[23] Y. Lion, E. Gandin, A. van de Vorst, *Photochem. Photobiol.* **1980**, *231*, 305.

[24] E. S. Shibu, M. Hamada, N. Murase, V. Biju, *J. Photochem. Photobiol., C* **2013**, *15*, 53.

[25] a) H. Arami, A. Khandhar, D. Liggitt, K. M. Krishnan, *Chem. Soc. Rev.* **2015**, *44*, 8576; b) Z. Liu, X. J. Liu, X. Ran, E. G. Ju, J. S. Ren, X. G. Qu, *Biomaterials* **2015**, *69*, 56; c) S. Sharifi, S. Behzadi, S. Laurent, M. L. Forrest, P. Stroeve, M. Mahmoudi, *Chem. Soc. Rev.* **2012**, *41*, 2323.